

Atomic collisions with relativistic heavy ions. V. The states of ions in matter

R. Anholt and W. E. Meyerhof

Department of Physics, Stanford University, Stanford, California 94305-2196

(Received 21 October 1985)

This paper examines the processes affecting relativistic heavy ions in solid targets. Three pieces of experimental information, the charge states of emergent projectiles, $K\alpha$ x-ray production cross sections, and K radiative electron-capture photon cross sections for 82- and 197-MeV/amu Xe projectiles incident on solid targets between Be and U, are examined. A theory incorporating the ground states and a minimal number of excited states of zero-, one-, and two-electron projectiles is formulated which includes capture, ionization, excitation, and decay processes. The requisite cross sections are obtained from calculations and measurements. The present charge-state, x-ray, and radiative capture photon measurements are in good agreement with theory. The relationship between charge-changing cross sections measured using thick and thin targets is examined.

I. INTRODUCTION

Because a sufficient number of cross sections can be accurately calculated with high-energy approximations, one of the advantages of studying atomic collisions with relativistic heavy ions is that one can develop an *ab initio* theory of the states of ions in matter. This can answer long-standing questions in atomic-collision physics regarding the role of excited states in determining the charge states of ions exiting solid or gas targets and the greater effectiveness of solid stripping foils over gas strippers.¹⁻³ Also, the formation of metastable states, which are important in beam-foil-spectroscopy studies, can be investigated.

It has always been possible to write down the rate equations governing the populations of ions of various charge states in their ground and excited states.^{1,2,4} However, the solution to these equations requires the calculation of a large number of ionization, excitation, capture, and decay cross sections. For several-electron ions, the number of requisite cross sections is excessively large. If there is any uncertainty in their magnitudes (which is always present given our poor understanding of nonradiative electron capture),¹ one cannot hope to accurately predict fine details such as differences between gas and solid strippers. Relativistic heavy ions have mainly zero, one, or two electrons (as long as the ion energy exceeds ~ 150 MeV/amu for Xe or ~ 400 MeV/amu for U).^{5,6} Hence, here we study mainly the stripping and excitation of $1s$, $2s$, or $2p$ electrons, which limits the number of required cross sections.

All together, five kinds of cross sections⁷⁻¹⁰ are needed to calculate the states of ions in matter. (1) Stripping or ionization cross sections were studied in papers I (Ref. 9) and IV (Ref. 10). It was found that for small perturbing fields, the cross sections could be calculated using the plane-wave Born approximation.^{4,11-13} Wave-function distortion effects¹⁴ are present for high perturbing charges. A modified empirical correction to the theory of Basbas *et al.*¹⁴ or the Glauber theory of ionization¹⁵ describes these effects adequately. (2) Cross sections for $1s$ -

$2s$ and $1s$ - $2p$ excitation^{4,16} are needed, which are expected to vary like the $1s$ ionization cross sections.^{17,18} Cross sections for $2s$ - $2p$ excitation can be calculated with the plane-wave Born approximation.⁴ (3) Radiative decay rates of excited states have been calculated for one- and two-electron ions of any atomic number.^{19,20} Auger decay is usually not present since doubly-excited-state configurations are rarely populated in the present high- Z ions. (4) Radiative electron-capture (REC) cross sections⁶⁻⁸ can be calculated accurately from photoelectric cross sections,²¹ leaving (5) nonradiative capture (NRC) cross sections, which are the most uncertain. The results of paper III (Ref. 8) showed that the eikonal approximation^{22,23} gives NRC cross sections which agree within about a factor of 2 or better with experiment for high- Z projectiles. However, this is still not good enough for the present detailed studies, so we will use measured NRC cross sections.

Four kinds of experimental information can be obtained about the states of ions in matter. The first is the charge states of ions exiting from gas targets or solid-target foils. In this paper the equilibrium charge states of 197-MeV/amu Xe ions are studied. Although the target-thickness dependence of the charge-state fractions were not measured in a way that can be directly compared with the present models, we discuss the relationship between charge-state fractions calculated including excited states and using ground-state models. Second, the cross sections for photons emitted when target electrons are radiatively captured into the projectile K shell give information about the number of projectile K vacancies present inside the solid target.⁷ Third, projectile $K\alpha$ x rays are mainly produced when $1s$ electrons are excited to vacant $2s$ or $2p$ states, hence the cross sections depend on the number of projectile $1s$ electrons present.²⁴ Finally, the production of metastable states, which are observable in principle by their radiative decay downstream of the target, can give direct information about the population of excited states of the projectile. As the latter quantities have not been measured for relativistic Xe ions, metastable-state formation is not discussed in this paper.

One of the purposes of the present paper is to examine

the role of excited states in determining the charge states and effective charge-changing cross sections of ions in solid targets. Therefore, an 11-state model of the states of ions in matter is constructed in a way which directly elucidates this role (Sec. III A). If excited states could be neglected (as is done in the ground-state model described in Sec. III B), the measured thin-target $1s$ single and double ionization¹⁰ and the measured $1s$ and excited-state capture cross sections⁸ would completely determine the equilibrium charge states of ions in matter. In fact, the ground-state model predicts He-like fractions that are higher than experiment for high- Z solid targets. The numerical 11-state model predicts the correct charge-state fractions using the same measured cross sections, but it also uses calculated excitation, decay, and excited-state stripping cross sections. An analytical quasiground-state model (Sec. III C) elucidates the reason why lower He-like fractions are seen in solid targets.

The close agreement between the measured equilibrium charge-state fractions (Sec. IV A), $K\alpha$ and REC photon cross sections (Sec. IV C), and the 11-state calculations validate the 11-state model. Therefore, we can use it to examine the relationship between charge-changing cross sections measured in thick versus thin targets (Sec. IV B). For this, we do "numerical experiments." The calculated zero-, one-, and two-electron charge-state fractions for various target thicknesses are treated like data. Least-squares fits of these data to solutions of the ground-state-model rate equations are made to obtain "best-fit" effective ionization and capture cross sections. We then compare the best-fit cross sections with the cross sections used as inputs in the 11-state model.

We compare the 11-state calculations with measured projectile $K\alpha$ and REC cross sections in Sec. IV C. Although the x-ray cross-section measurements were discussed in paper I (Ref. 9) and Ref. 7, several aspects of the measurement of projectile K x rays, not present when target K x rays are measured, must be considered (Sec. II). Conclusions are given in Sec. V.

In this paper the projectile atomic number is denoted by Z_p and the target by Z_t , and β is the projectile velocity relative to the speed of light.

II. EXPERIMENT

The apparatus and methods used to measure target K x-ray production, projectile K x-ray production, and REC photons were described in paper I.⁹ Several points should be reiterated. First, thick targets were used in all measurements. It was verified that for the thicknesses used, the measured x-ray cross sections are independent of the target thickness. Therefore, the calculations described in Sec. III are for the equilibrium $K\alpha$ x-ray production cross sections. In addition, the incident projectile charge states were fixed by the presence of a 180-mg/cm²-thick, transmission-mounted, silicon surface barrier upstream from the target. This brought the incoming projectile charge states to the equilibrium values for $Z_t = 14$, which is already close to that of most target materials. X rays from the upstream and downstream particle detectors and other potential background sources were not observed.⁹

The projectile x rays are Doppler shifted with laboratory angle θ_{lab} and their angular distribution varies as

$$\frac{d\sigma}{d\Omega} = \frac{d\sigma(90^\circ)}{d\Omega} \frac{1}{(1 - \beta \cos\theta_{\text{lab}})^2}, \quad (1)$$

where βc is the ion velocity. Figure 1 shows the energy and angular distribution of projectile La $K\alpha$ x rays in 174-MeV/amu La + Be collisions. Since the La ion is nearly fully stripped, the rest-frame x-ray energy is given by the Dirac equation

$$E_{K\alpha} = \{ [1 - (Z_p\alpha/2)^2]^{1/2} - [1 - (Z_p\alpha)^2]^{1/2} \} mc^2, \quad (2)$$

and the laboratory energy varies as

$$E_x = E_{K\alpha} \gamma^{-1} (1 - \beta \cos\theta_{\text{lab}})^{-1}, \quad (3)$$

where $\gamma = (1 - \beta^2)^{-1/2}$. Usually, only the x-ray cross sections $\sigma(90^\circ)$ (in units of barns/4 π sr) at $\theta_{\text{lab}} = 90^\circ$ were measured. The desired total x-ray production cross sections are then given by

$$\sigma_{K\alpha} = \sigma(90^\circ) (1 - \beta^2)^{-1}. \quad (4)$$

In the present measurements for 82- and 197-MeV/amu Xe ions, the net relative uncertainties in the $K\alpha$ x-ray cross sections are approximately $\pm 12\%$, omitting counting-statistics uncertainties. (Sources of the experimental uncertainties are discussed in paper I.⁹) The major uncertainties contributing to the statistical errors result from the subtraction of the intense continuum x-ray backgrounds present when relativistic heavy ions are used.²⁴

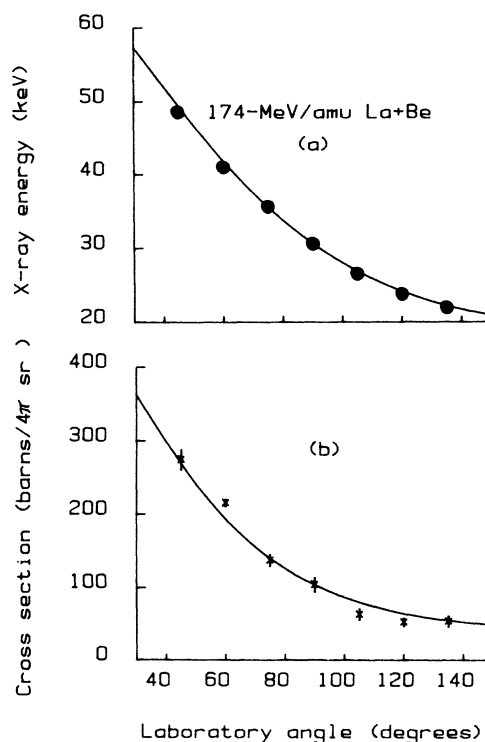


FIG. 1. Projectile $K\alpha$ x-ray energies (a) and cross sections (b) plotted against laboratory angle for 174-MeV/amu La + Be collisions.

These fundamental backgrounds, due to primary- and secondary-electron bremsstrahlung, could not be reduced significantly in the present experimental arrangement. Only the $K\alpha$ cross sections are reported here. $K\beta$ x-ray production would be interesting to compare with an extended theory, but, due to the high x-ray background, accurate cross sections could not be obtained.

III. MODELS OF THE STATES OF IONS IN MATTER

A. The 11-state model

We have previously described a model for calculating the states of low- Z relativistic ions in gas and solid targets.⁴ There, only zero- and one-electron states had to be included. The fraction of projectiles bearing an electron was less than 10^{-3} ; therefore, the fraction bearing two electrons was immeasurably small.²⁵ For high- Z ions, the one-electron fractions are generally greater than 10^{-1} , and two-electron fractions greater than 10^{-2} were observed. For low- Z ions, it was sufficient to include in this model only the $1s$, $2s$, and $2p$ states. For high- Z ions we shall include, in addition, the $1s^2$, $1s2s$, and $1s2p$ configurations. We shall not attempt to calculate $K\beta$ x-ray yields which would require $3s$, $3p$, $4s$, $4p$, $1s3s$, $1s3p$, $1s4s$, and $1s4p$ configurations. Since the $3s$ and $3p$ configurations do not contribute much to the charge-state fractions of low- Z projectiles,⁴ these states should not contribute significantly to the charge states of high- Z , one- or two-electron ions (although including such states would greatly refine this model). Since the calculated relative excited-state populations are found to be small, doubly excited states can be neglected.

With this minimal model, one has the 11 states shown in Fig. 2. The $1s2s$ configuration gives the 1S_0 and 3S_1 states, and the $1s2p$ configuration gives four states, 1P_1 ,

3P_0 , 3P_1 , and 3P_2 , which, due to their diverse decay rates,²⁰ must be calculated separately. We denote the $(1s2s)2^1S_0$ state by 1S_0 and the $(1s^2)1^1S_0$ state by $1s^2$. Also, we refer to the bare ion as the $1s^0$ state.

The rate of change of the population of these states is determined by cross sections for capture (a_i), for stripping (s_i), for decay (d_i), for excitation (x_i), and for double-electron ionization (c_i). For example, a_1 is the cross section for the capture of electrons from any shell of the fully occupied target atom into the empty projectile K shell. If capture occurs into the projectile state where a $1s$ electron is already present, the cross section is $a_1/2$. Similarly, a_2 is the cross section for capture into the projectile $2s$ state and a_3 is the $2p$ capture cross section. For capture into the 3S_1 state from the $1s$ state, one uses $3a_2/4$, since the probability is three times larger for capture into a triplet state than for capture into the singlet 1S_0 state. Similar considerations govern the relative capture probabilities into the $1s2p$ states. Our model assumes that the presence of a $1s$ electron does not significantly affect the total capture cross section, so that the sum of the $1s \rightarrow ^1S_0$ and $1s \rightarrow ^3S_1$ cross sections is equal to the hydrogenic $2s$ capture cross section. This assumption should be valid for the high- Z projectiles used. Since no experimental evidence of double-electron capture is available for 197-MeV/amu Xe projectiles (and no theory of double capture is available),⁸ we neglect double-capture transitions.

The $1s$ ionization cross section is denoted by s_1 , and the $2s$ and $2p$ ionization cross sections are denoted by s_2 and s_3 . Since the ionization cross sections are defined per electron, the $1s^2$ single-electron ionization cross section is twice as large as the $1s$ one. In the He-like excited states, either the $n=1$ ($1s$) or $n=2$ ($2s$ or $2p$) electrons can be ionized. We also assume that the presence of an additional electron does not affect the two-electron cross sections much, so that, for example, the cross section for $1s2s \rightarrow 1s$ is equal to the hydrogenic $2s$ ionization cross section.

Paper IV (Ref. 10) showed that projectile double-electron ionization is significant for large target atomic numbers, hence the cross sections c_1 , c_2 , and c_3 for $1s^2$, $1s2s$, and $1s2p$ double ionization have been included in this model.

Three radiative decay rates are very large for Xe ions: the $2p \rightarrow 1s$ ($\lambda_1 = 5.3 \times 10^{15} \text{ sec}^{-1}$),¹⁹ the $^1P_1 \rightarrow 1s^2$ ($\lambda_2 = 6.8 \times 10^{15} \text{ sec}^{-1}$),²⁰ and the $^3P_1 \rightarrow 1s^2$ ($\lambda_3 = 3 \times 10^{15} \text{ sec}^{-1}$) rates.²⁰ The $^3P_1 \rightarrow 1s^2$ spin-forbidden transition rate is not large for low- Z ions, but is large at high Z , due to spin-orbit coupling, where it corresponds to the $1s2p_{1/2} \rightarrow 1s^2$ transition. The radiative decay cross sections shown in Fig. 2 are given by

$$d_i = \frac{\lambda_i}{n_2 \gamma \beta c}, \quad (5)$$

where λ_i is the transition rate, and n_2 is the target-atom density. All other radiative transitions need not be included in solid targets since the corresponding radiative decay cross sections add negligibly to collisional deexcitation cross sections.

Collisional excitation and deexcitation can occur. In the one-electron states, x_1 is the $1s$ - $2s$ and x_2 is the $1s$ - $2p$ excitation cross section. An excited electron can be col-

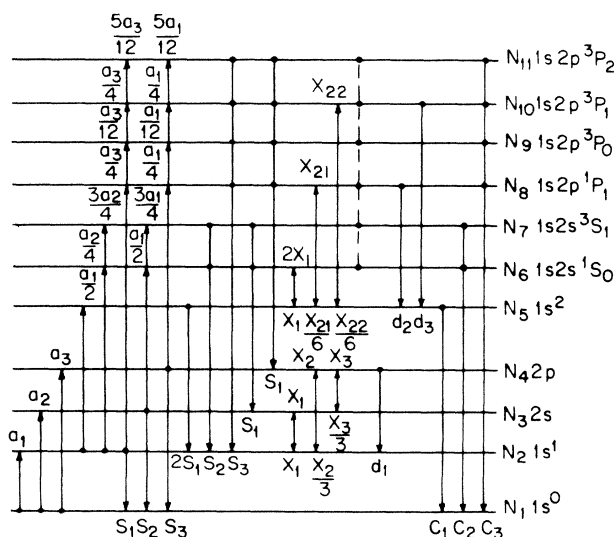


FIG. 2. Schematic level diagram showing transitions between the 11 states included in the present model. The quantities a_i represent capture cross sections; s_i , projectile ionization cross sections; x_i , excitation cross sections; d_i , radiative decay cross sections; and c_i , double-ionization cross sections.

TABLE I. Cross-section matrix (A_{ij}) in the rate-of-change equations for the level population [Eq. (6)]. The entries on the diagonal, A_{ii} , are given by -1 times the sum of all off-diagonal entries in column i ; for example, $A_{22} = -(s_1 + x_1 + x_2 + \frac{1}{2}a_1 + a_2 + a_3)$. Here, $t \equiv n_2 T$.

$N_1(\text{bare})$	$A_{1,1}$	s_1	s_2	s_3	c_1	c_2	c_2	c_3	c_3	c_3	c_3	$N_1(\text{bare})$
$N_2(1s)$	a_1	$A_{2,2}$	x_1	$x_2/3 + d_1$	$2s_1$	s_2	s_2	s_3	s_3	s_3	s_3	$N_2(1s)$
$N_3(2s)$	a_2	x_1	$A_{3,3}$	$x_3/3$	0	s_1	s_1	0	0	0	0	$N_3(2s)$
$N_4(2p)$	a_3	x_2	x_3	$A_{4,4}$	0	0	0	s_1	s_1	s_1	s_1	$N_4(2p)$
$N_5(1s^2)$	0	$a_1/2$	0	0	$A_{5,5}$	x_1	0	$1.4x_2/6 + d_2$	0	$d_3 + 0.6x_2/6$	0	$N_5(1s^2)$
$N_6(^1S_0)$	0	$a_2/4$	$a_1/4$	0	$2x_1$	$A_{6,6}$	0	$x_4/3$	0	$x_8/3$	0	$N_6(^1S_0)$
$N_7(^3S_1)$	0	$3a_2/4$	$3a_1/4$	0	0	0	$A_{7,7}$	x_9	$3x_5$	x_6	$3x_7/5$	$N_7(^3S_1)$
$N_8(^1P_1)$	0	$a_3/4$	0	$a_1/4$	$1.4x_2$	x_4	x_9	$A_{8,8}$	0	0	0	$N_8(^1P_1)$
$N_9(^3P_0)$	0	$a_3/12$	0	$a_1/12$	0	0	x_5	0	$A_{9,9}$	0	0	$N_9(^3P_0)$
$N_{10}(^3P_1)$	0	$a_3/4$	0	$a_1/4$	$0.6x_2$	x_8	x_6	0	0	$A_{10,10}$	0	$N_{10}(^3P_1)$
$N_{11}(^3P_2)$	0	$5a_3/12$	0	$5a_1/12$	0	0	x_7	0	0	0	$A_{11,11}$	$N_{11}(^3P_2)$

tionally deexcited to the $1s$ state with cross section x_1 ($2s \rightarrow 1s$) or $x_2/3$ ($2p \rightarrow 1s$). The factor $\frac{1}{3}$ takes into account the relative density of final states in the inverse process. The $1s^2$ two-electron states are excited with twice the single-electron $1s \rightarrow 2s$ and $1s \rightarrow 2p$ excitation cross sections. $1s^2 \rightarrow 1s2p$ excitation populates the 1P_1 and 3P_1 states, with relative cross sections $x_{21} = 1.4x_2$ for the 1P_1 state and $x_{22} = 0.6x_2$ for the 3P_1 state (see Sec. III D 4 below). The $2s \rightarrow 2p$ excitation cross section is denoted by x_3 . The $1s2s \rightarrow 1s2p$ cross sections are discussed in Appendix A.

The equations for the rate of change of the populations of the various levels can be derived from Fig. 2. One has

$$\dot{N}_i = \sum_{j=1}^{11} A_{ij} N_j(T), \quad (6)$$

where the cross-section matrix A_{ij} is given in Table I, $\dot{N} = dN/d(n_2 T)$, and T is the target thickness. The equilibrium populations are obtained by setting the derivatives equal to zero and solving the resulting set of 11 simultaneous linear equations. The total one-electron charge-state fraction F_1 is given by the sum of the $1s$, $2s$, and $2p$ populations, and the total two-electron charge-state fraction F_2 is the sum of the seven He-like state populations (N_5, N_6, \dots, N_{11}).

Most $K\alpha$ x rays are emitted inside the target.^{4,26} The equilibrium $K\alpha$ x-ray production cross section is given by

$$\sigma_{K\alpha} = d_1 N(2p) + d_2 N(^1P_1) + d_3 N(^3P_1), \quad (7)$$

where $N(2p)$ is the equilibrium $2p$ population, and the decay cross sections d_i are given by Eq. (5).

B. The ground-state model

Comparison is made in this paper with the ground-state model which assumes that the excited states decay instantaneously to the ground state. In this model, the rate equations for the charge-state fractions F_i , where i is the number of electrons, are given by

$$\begin{aligned} \dot{F}_0 &= -(a_1 + a_2 + a_3)F_0 + s_1 F_1 + c_1 F_2, \\ \dot{F}_1 &= (a_1 + a_2 + a_3)F_0 - (s_1 + \frac{1}{2}a_1 + a_2 + a_3)F_1 + 2s_1 F_2, \\ \dot{F}_2 &= (\frac{1}{2}a_1 + a_2 + a_3)F_1 - (c_1 + 2s_1)F_2, \end{aligned} \quad (8)$$

where $\dot{F}_i = dF_i/d(n_2 T)$, and the cross sections are the same as in Fig. 2 or Table I. The equilibrium charge-state fractions are given by²⁷

$$F_0 = [1 + \alpha(1 + \beta)]^{-1}, \quad F_2 = \beta F_1, \quad F_1 = \alpha F_0, \quad (9)$$

$$\alpha = \frac{a_1 + a_2 + a_3}{s_1 + \beta c_1}, \quad \beta = \frac{\frac{1}{2}a_1 + a_2 + a_3}{2s_1 + c_1}.$$

The ground-state model should be valid in gas targets where, due to the low target-atom densities n_2 , the decay cross sections are enormous compared to all other cross sections (even for the neglected weaker $E1$ and higher-multipole transitions by which the $2s$, $1s2s$, 3P_0 , and 3P_2 states decay). Therefore, all excited-state populations are near zero, and one can assume that all capture effectively goes into the ground state.

C. The quasiground-state model

1. Equilibrium charge states

The results in Sec. IV show that the excited-state populations in high- Z ions tend to be much smaller than the respective ground-state populations. Our quasiground-state model assumes that the populations of the $1s^0$, $1s$, and $1s^2$ states are approximately equal to the charge-state fractions F_0 , F_1 , and F_2 . In each equation for a given equilibrium excited-state population, e.g.,

$$\begin{aligned} \dot{N}_3 = \dot{N}(2s) = 0 &= a_2 N(1s^0) + x_1 N(1s) \\ &\quad - (s_2 + x_1 + x_3 + a_1) N(2s) \\ &\quad + \frac{1}{3} x_3 N(2p) + s_1 (N(^1S_0) + N(^3S_1)), \end{aligned} \quad (10)$$

we set the other excited-state populations equal to zero and obtain

$$N(2s) \approx \frac{a_2 F_0 + x_1 F_1}{s_2 + x_1 + x_3 + a_1}. \quad (11)$$

Now consider the equation for \dot{F}_2 :

$$\begin{aligned} \dot{F}_2 = 0 = \sum_{i=5}^{11} \dot{N}_i &= \left(\frac{1}{2}a_1 + a_2 + a_3\right)N(1s) + a_1 N(2s) \\ &+ a_1 N(2p) - (2s_1 + c_1)N(1s^2) \\ &- (s_2 + s_1 + c_2)(N_6 + N_7) \\ &- (s_3 + c_3 + s_1)(N_8 + N_9 + N_{10} + N_{11}). \end{aligned} \quad (12)$$

We neglect the excited-state terms $N(2s)$ and $N(2p)$, substitute $N(1s^2) = F_2$ and $N(1s) = F_1$, and the solutions for N_6 through N_{11} obtained as in Eq. (11). We then have an equation in terms of just F_1 and F_2 which we can solve for the equilibrium ratio

$$\frac{F_2}{F_1} = \frac{a_1/2 + a_2 r_2 + a_3 r_3}{(2s_1 + c_1)r_s}, \quad (13)$$

where

$$\begin{aligned} r_2 &= 1 - \frac{s_{22}}{4} \left[\frac{3}{s_{22} + x_5 + x_6 + x_7 + x_9} + \frac{1}{s_{22} + x_1 + x_4 + x_8} \right], \\ r_3 &= 1 - \frac{s_{33}}{12} \left[\frac{3}{s_{33} + d_2 + x_9 + x_4/3 + 1.4x_2/6} + \frac{1}{s_{33} + 3x_5} + \frac{3}{s_{33} + x_6 + d_3 + x_8/3 + 0.1x_2} + \frac{5}{s_{33} + 3x_7/5} \right], \end{aligned} \quad (14)$$

and

$$r_s = 1 + \left[\frac{1.4x_2 s_{33}}{s_{33} + d_2 + x_9 + x_4/3 + 1.4x_2/6} + \frac{0.6x_2 s_{33}}{s_{33} + d_3 + x_6 + x_8/3 + 0.1x_2} + \frac{2x_1 s_{22}}{s_{22} + x_1 + x_4 + x_8} \right] (2s_1 + c_1)^{-1},$$

$$s_{22} = s_2 + s_1 + c_2, \quad s_{33} = s_3 + s_1 + c_3.$$

In the ground-state model, r_2 , r_3 , and r_s are equal to unity, so that F_2/F_1 then is equal to β in Eq. (9).

Numerical results show that for the present high- Z ions, excited-state effects are most visible in the F_2 fractions. The measured F_2/F_1 ratios are smaller than the ground-state values mainly because (1) due to excited-electron ionization, not all of the capture into excited states counts in determining F_2 ($r_2, r_3 < 1$), and (2) the effective $1s$ ionization cross sections are slightly larger than $2s_1 + c_1$ ($r_s > 1$). The reduction in the capture cross sections is more significant than the increase in the ionization cross sections. For 197-MeV/amu Xe + Ag collisions, one obtains the following from the cross sections discussed below: $r_2 = 0.534$, $r_3 = 0.625$, and $r_s = 1.08$. This gives $F_2/F_1 = 0.144$ instead of $\beta = 0.197$ in the ground-state model. The numerical 11-state-model results discussed in Sec. IV A give $F_2/F_1 = 0.140$, in good agreement with the quasiground-state result. The effective $1s$ ionization cross section is not increased significantly for high- Z ions, since dipole $1s \rightarrow 2p$ excitation populates states which decay quickly back to the ground state, producing no change in the projectile charge state. Most of the 8% increase in the effective $1s$ ionization cross sections for 197-MeV/amu Xe collisions comes from monopole $1s$ - $2s$ excitation, which is not followed by rapid decay. The main reduction in F_2 below the ground-state values is due to capture into the metastable $2s$, 1S_0 , 3S_1 , 3P_0 , and 3P_2 states which decay slowly by $2s$ - $2p$ excitation, hence are likely to be ionized. Since the r_2 and r_3 values are neither zero nor unity, one can neither assume a ground-state model nor that the metastable states do not decay at all.

2. Equilibrium x-ray production

To calculate $K\alpha$ x-ray production in the quasiground-state model, we need in Eq. (7) the $2p$, 1P_1 , and 3P_1 populations. Following the arguments leading to Eq. (11), we obtain

$$\begin{aligned} N(2p) &= \frac{a_3 F_0 + x_2 F_1 + x_3 N(2s)}{s_3 + d_1 + a_1 + (x_2 + x_3)/3}, \\ N(^1P_1) &= \frac{a_3/4 F_1 + 1.4x_2 F_2 + x_4 N(^1S_0) + x_9 N(^3S_1)}{s_3 + s_1 + d_2 + c_3 + x_9 + (x_2 + x_4)/3}, \\ N(^3P_1) &= \frac{3a_3/12 F_1 + 0.6x_2 F_2 + x_8 N(^1S_0) + x_6 N(^3S_1)}{s_3 + s_1 + d_3 + c_3 + x_6 + x_8/3}. \end{aligned} \quad (15)$$

Unlike for equilibrium charge states, we cannot neglect the $1s2s$ and $2s$ populations since, due to the large $2s \rightarrow 2p$ transfer cross sections, these will contribute significantly to $K\alpha$ x-ray production. Substituting the remaining populations, we obtain for the equilibrium $K\alpha$ x-ray production cross sections

$$\begin{aligned} \sigma_{K\alpha} &= \omega_1 a_3 F_0 + \frac{a_3}{4} F_1 (\omega_2 + \omega_3) + \omega_1 x_2 F_1 \\ &+ x_2 F_2 (1.4\omega_2 + 0.6\omega_3) + \omega_1 \omega_{2s} a_2 F_0 \\ &+ \omega_{1s2sc} a_2 F_1 + \omega_1 \omega_{2s} x_1 F_1 + \omega_{1s2sx} 2x_1 F_2, \end{aligned} \quad (16)$$

where

$$\begin{aligned}
\omega_1 &= d_1(s_3 + d_1 + a_1 + (x_2 + x_3)/3)^{-1}, \\
\omega_2 &= d_2(s_3 + s_1 + d_2 + c_3 + x_9 + (x_2 + x_4)/3)^{-1}, \\
\omega_3 &= d_3(s_3 + s_1 + d_3 + c_3 + x_6 + x_8/3)^{-1}, \\
\omega_{2s} &= x_3(s_2 + x_1 + x_3 + a_1)^{-1}, \\
(\omega_{x_4}, \omega_{x_8}) &= (x_4, x_8)(s_2 + s_1 + c_2 + x_1 + x_4 + x_8)^{-1}, \\
(\omega_{x_6}, \omega_{x_9}) &= (x_6, x_9)(s_2 + s_1 + c_2 + x_5 + x_6 + x_7 + x_9)^{-1}, \\
\omega_{1s2sx} &= \omega_2\omega_{x_4} + \omega_3\omega_{x_8},
\end{aligned}
\tag{17}$$

and

$$\omega_{1s2sc} = \frac{1}{4}(\omega_2\omega_{x_4} + 3\omega_2\omega_{x_9} + 3\omega_3\omega_{x_6} + \omega_3\omega_{x_8}).$$

This lengthy equation has the following physical interpretation. The $2p$ and $1s2p$ populations lead to the emission of an x ray if the radiative decay cross sections d_i are much larger than the $2p$ -ionization s_3 , deexcitation, and all other cross sections by which the $2p$, 1P_1 , and 3P_1 states decay. Hence the ratios ω_i are solid-target fluorescence yields. The $2p$ state is populated by capture into bare projectiles (term a_3F_0). If the projectile already has a $1s$ electron, only those electrons captured into the $2p$ orbital of opposite spin emit x rays, hence one obtains the term $\frac{1}{2}a_3F_1$ in the limit where ω_2 and ω_3 are unity. Electrons in the $1s$ and $1s^2$ states can be excited to the $2p$ state with cross sections x_2F_1 and $2x_2F_2$ (for $\omega_2 = \omega_3$). Since $1s \rightarrow 2p$ excitation does not change the spin of the electron, dipole radiative decay back to the ground state is allowed and will occur depending on the fluorescence yields ω_i . Electrons in the $2s$ or $1s2s$ states, populated by capture (terms a_2F_0 and a_2F_1) or monopole $1s$ - $2s$ excitation (terms x_1F_1 and $2x_1F_2$), can be excited to the decaying $2p$ state. The ratios ω_{2s} and $\omega_{1s2sc,x}$ give the probability of $2s \rightarrow 2p$ excitation to the emitting state before $2s$ ionization or deexcitation occurs.

For 82-MeV/amu Xe ions, significant fractions of three- and four-electron ions are present. Having understood the physical origin of the various terms in Eq. (16), we can extend this model to include three- and four-electron projectiles without resorting to extensive coupled-state formulations. We shall not attempt to calculate the charge-state fractions F_3 and F_4 ; only the equilibrium $K\alpha$ x-ray production cross sections are calculated from the measured equilibrium ratios. For projectiles with three or more (active) electrons, $2p$ and $2s$ capture no longer plays a role, because the $1s$ orbitals are normally filled, hence the captured electrons cannot decay radiatively. Another mechanism then appears: $1s$ ionization. If $1s$ ionization of the three-electron $1s^22p$ state occurs, the $2p$ electron can decay to the $1s$ level if it has the right spin. This, of course, is the main mechanism for the production of projectile K x rays in many-electron projectiles. To keep this model tractable, we omitted the monopole $1s \rightarrow 2s$ excitation cross sections and included only $1s \rightarrow 2p$ excitation and $1s$ ionization. The model is discussed further in Appendix B. We obtain, for the total $K\alpha$ x-ray production cross sections, that given in Eq. (16) plus

$$\Delta\sigma_{K\alpha} = \frac{3}{8}s_1(\omega_3 + \omega_2)F_3 + \frac{7}{4}x_2\omega_1F_3 + \frac{3}{2}\omega_1x_2F_4 + 2s_1F_4. \tag{18}$$

D. Cross sections

Fifteen fundamental cross sections, $s_1, s_2, s_3, x_1, x_2, x_3, a_1, a_2, a_3, c_1, c_2, c_3, d_1, d_2,$ and d_3 , are needed in the 11-state and quasiground-state models. Only four, $a_1, a_2 + a_3, c_1,$ and s_1 , are needed in the ground-state model. We shall proceed by taking the four ground-state cross sections from experiment.^{8,10} We calculate the remaining cross sections absolutely or relatively using the Born^{10-13,16} or semiclassical²⁸ approximations for excitation and ionization, the eikonal approximation²³ for non-radiative electron capture, and the impulse approximation⁷ for radiative electron capture. This has two advantages. First, the ground-state cross sections tend to be the least well understood. Because the ratio of the ion velocity to the electron velocity is much greater than unity for the L -shell electrons, we expect that distortion effects are less important. Hence, the Born approximation should give more accurate L -shell ionization and $2s \rightarrow 2p$ excitation cross sections than $1s$ ionization cross sections.¹⁰ The eikonal approximation can be used to calculate the ground-state NRC cross sections within factors of about 2,⁸ but this is not sufficiently accurate for the present model, where we hope to explain 20%–60% differences in some measured and calculated zero-, one-, and two-electron charge-state fractions. The second advantage of this approach is that one can isolate the excited-state effects. The four measured cross sections were determined using thin targets, where excitation plays no role. If one calculates the equilibrium charge states using the ground-state model and the four measured cross sections, the deviation from experiment is a direct measure of excited-state effects, which the 11-state model attempts to explain.

1. Ionization

Figure 3 shows $1s$ and $2s$ ionization cross sections. The measured $1s$ ionization cross sections were obtained from thin-target measurements and are discussed in paper IV.¹⁰ At small Z_t , the measured ionization cross sections are larger than the Born-approximation predictions. At large Z_t , they are smaller, due to wave-function distortion or unitarity effects.^{14,15} The $2s$ and $2p$ ionization cross sections were calculated using the plane-wave Born approximation (PWBA) including target-electron screening and antiscreening as discussed in papers II (Ref. 4) and IV (Ref. 10). We noted in paper I (Ref. 9) that the target L x-ray cross sections in Xe + (Ta–U) collisions could be calculated accurately using the PWBA. Since for Xe L -shell ionization the projectile velocity relative to the L -electron velocity is larger than for the Ta–U targets, the PWBA should be even more accurate for Xe projectile L -shell ionization. The calculated $2s$ ionization cross sections are much larger than the $1s$ ionization ones, as shown in Fig. 3. The $2p$ ionization cross sections are about 30% larger per electron than the $2s$ ionization cross sections.

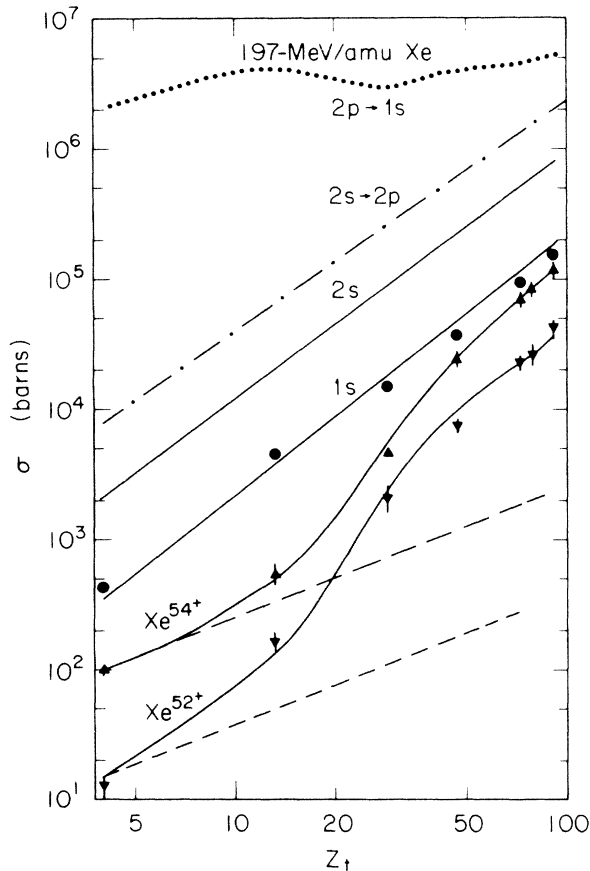


FIG. 3. Calculated cross sections for $2p \rightarrow 1s$ radiative decay (dotted line), $1s$ and $2s$ ionization (solid lines), $2s \rightarrow 2p$ excitation (dot-dashed line), and REC (dashed lines) for 197-MeV/amu Xe collisions. The measured $1s$ ionization cross sections are shown by closed circles, and measured Xe^{54+} and Xe^{52+} electron-capture cross sections are shown by triangles (with connecting solid lines to guide the eye).

2. Double ionization

The $1s^2$ double-electron ionization cross sections c_1 were taken from experiment. Paper IV showed that they could be calculated approximately using

$$c_1 = \int_0^\infty db 2\pi b P_{1s}(b) P_{1s}(b), \quad (19)$$

where $P_{1s}(b)$ is the semiclassical ionization probability²⁸ at impact parameter b . For $1s2s$ double ionization, one can replace one factor of P_{1s} with P_{2s} and similarly do so for $1s2p$ double ionization. To obtain c_2 and c_3 , we calculated the $1s2s$ and $1s2p$ double ionization cross sections relative to the $1s^2$ cross section using the semiclassical approximation and normalized to the measured value of c_1 .

3. Capture cross sections

Measured cross sections for electron capture by Xe^{54+} and Xe^{52+} ions were used (Fig. 3).⁸ To calculate equilibrium charge states, we assumed that the cross sections a_1 and $a_2 + a_3$ are given by

$$a_1 = \sigma(\text{Xe}^{54+}) - \sigma(\text{Xe}^{52+}), \quad (20)$$

$$a_2 + a_3 = \sigma(\text{Xe}^{52+}).$$

Unfortunately, approximately 50% of the Xe^{52+} electron capture at high Z_t goes into the $n=3, 4, \dots$ states which are not included in the present model.^{8,23} By assuming that all of the Xe^{52+} electron capture goes into the $n=2$ state, we are modeling the $n=3$ and higher states by the $n=2$ states.

The implications of this assumption can be seen by examining the equations for r_2 and r_3 , Eqs. (14). If we neglect the $n=2$ to $n=3$ excitation and decay cross sections, we can derive similar equations for the factors r'_2 and r'_3 multiplying the $3s$ and $3p$ capture cross sections. The terms involving radiative decay cross sections tend to be negligible, so that r'_2 and r'_3 are given by ratios of excited-state ionization cross sections to ionization plus $1sns-1snp$ excitation cross sections. For higher shells, the ionization and excitation cross sections are both larger than the $n=2$ ones, but the ratios r_2 and r_3 should not change significantly with n , implying that similar r_2 and r_3 values for capture into the $n=2$ and higher shells should be obtained. If this is true, modeling capture into $n \geq 3$ states by capture into $n=2$ states should be valid.

To calculate a_2 and a_3 separately, we took the relative $2s$ and $2p$ cross sections from the eikonal approximation²³ for NRC and the impulse approximation⁷ for REC.

When we calculate $K\alpha$ x-ray production, we cannot assume that all Xe^{52+} capture goes into the $n=2$ states since the capture into $n=3$ and higher states contributes to $K\beta$ x-ray production. Thus, here we calculated the relative contributions into the $2s$ and $2p$ states using the eikonal or impulse approximations, normalized to the measured Xe^{52+} cross sections, and added to a_1 the remaining part of the Xe^{52+} cross sections, representing capture into the $n=3$ and higher states.

4. Excitation cross sections

We calculated the $1s \rightarrow 2s$ and $1s \rightarrow 2p$ cross sections relative to the $1s$ ionization cross sections using the PWBA (Ref. 16) including target-electron screening.⁴ The dipole $1s \rightarrow 2p$ cross section is about 0.7 times the $1s$ ionization cross section for 197-MeV/amu Xe + Be collisions, and the $1s \rightarrow 2s$ cross section is about 0.09 times the $1s$ ionization one. Target-electron screening reduces the $1s \rightarrow 2p$ cross sections more significantly than ionization. For instance, the $1s \rightarrow 2p$ excitation cross section at $Z_t=92$ is 0.62 times the ionization one. We assume that wave-function distortion effects^{14,15} affect the $1s \rightarrow 2p$ excitation, $1s \rightarrow 2s$ excitation, and $1s$ ionization cross sections equally. Then one can use the PWBA ratios and normalize to the measured $1s$ ionization cross sections. We checked this assumption by examining ratios of measured $p + \text{H}$ $1s$ ionization^{10,18} and $n=2$ excitation¹⁷ cross sections to the PWBA predictions for (25–50)-keV protons. They are approximately equal at every proton energy within experimental uncertainties. Since we have also noted that the $\text{Xe}^{53+} + \text{Xe}$ $1s$ ionization cross sections for 82 and 197 MeV/amu agree with scaled $p + \text{H}$ ones at 25 and 50 keV,¹⁰ we conclude that the $1s \rightarrow 2p$ excitation

cross sections should agree also, if one corrects for target screening effects using the PWBA.

For $1s^2 \rightarrow 1s2p$ excitation, the relativistic effects that give large $^3P_1 \rightarrow ^1S_1$ decay rates²⁰ will likewise affect the dipole excitation cross sections. Since similar matrix elements enter at the small q values contributing most to the excitation cross sections, we took the relative cross sections from the decay rates.²⁰ Therefore, in Fig. 2 we have

$$\sigma(1s^2 \rightarrow ^1P_1) = x_{21} \sim 1.4x_2, \quad (21)$$

$$\sigma(1s^2 \rightarrow ^3P_1) = x_{22} \sim 0.6x_2.$$

The sum adds up to $2x_2$, because there are two $1s$ electrons that can be excited. The deexcitation cross sections are given by

$$\sigma(^1P_1 \rightarrow 1s^2) = \frac{1}{6}\sigma(1s^2 \rightarrow ^1P_1), \quad (22)$$

where the factor of $\frac{1}{6}$ accounts for the smaller density of final states.

The $2s$ - $2p$ excitation cross sections were calculated absolutely using the PWBA including target-electron screening and Dirac wave functions. The $1s2s$ - $1s2p$ excitation cross sections are discussed in Appendix A. Preliminary results of Betz²⁹ indicate possible discrepancies between measured $2s$ - $2p$ excitation cross sections and PWBA calculations. The consequences of such discrepancies in the present work can only be examined after those results are confirmed.

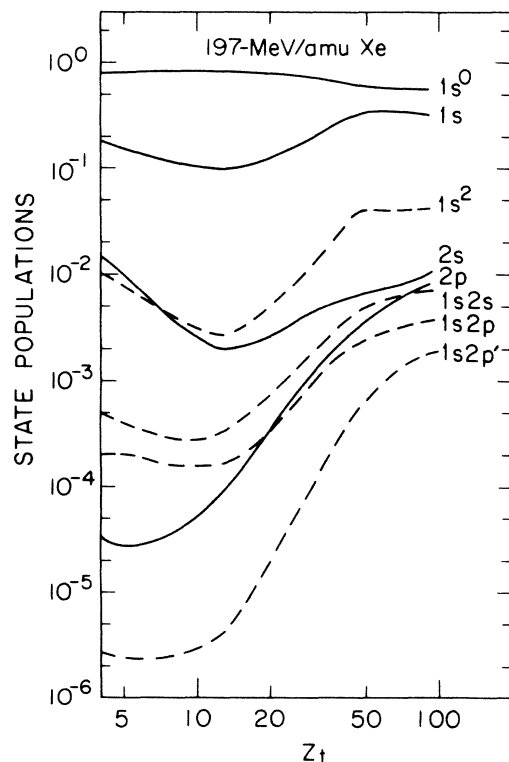


FIG. 4. Calculated equilibrium state populations in 197-MeV/amu Xe ions. To keep the number of curves in this figure small, some populations which have similar Z_t dependences have been summed. The $1s2s$ population is the sum of the 1S_0 and 3S_1 ones, the $1s2p$ is the sum of the 3P_0 and 3P_2 ones, and the $1s2p'$ is the sum of the 1P_1 and 3P_1 ones.

IV. RESULTS

A. Equilibrium charge-state fractions

Figure 4 shows the calculated equilibrium populations of states of 197-MeV/amu Xe projectiles. Due to large radiative decay rates in these high- Z ions, the excited-state populations are generally much smaller than the respective ground-state $1s^0$, $1s$, or $1s^2$ populations. The rapidly decaying $2p$ and $1s2p'$ (sum of 1P_1 and 3P_1) states have the smallest populations at low Z_t . At large Z_t , where the capture and ionization cross sections become comparable to the radiative decay cross sections (Fig. 3), relatively high $2p$ and $1s2p'$ populations are found. The metastable $2s$ and $1s2s$ (sum of 1S_0 and 3S_1) states decay by $2s$ - $2p$ excitation to the $2p$, 1P_1 , and 3P_1 states. Since the $2s \rightarrow 2p$ excitation cross sections are large, but generally not as large as the radiative decay cross sections, these populations are greater than the $2p$ populations but much less than the $1s$ and $1s^2$ ones, respectively. The $1s2p$ (sum of 3P_0 and 3P_2) states decay by $2p \rightarrow 2s$ deexcitation to the 3S_1 and 1S_0 states, which in turn decay by $2s \rightarrow 2p$ excitation to the 1P_1 and 3P_1 states.

Figure 5 shows the equilibrium charge-state fractions

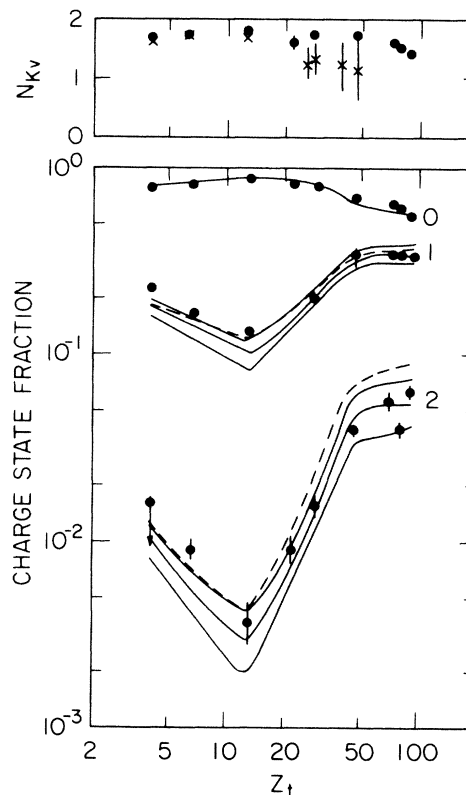


FIG. 5. Measured and calculated charge-state fractions for 197-MeV/amu Xe collisions. The experimental uncertainties in the ionization and capture cross sections shown in Fig. 3 give uncertainties in the calculated charge-state fractions extending from the lower to upper solid lines. The ground-state model (dashed lines) should be compared with the middle solid lines, based on the most likely NRC cross sections. The uppermost figure compares the number of projectile K vacancies obtained from the charge-state measurements ($2F_0 + F_1$, closed circles) with the REC photon measurements [Eq. (25), crosses].

for 197-MeV/amu Xe ions. The uncertainties in the measured ground-state cross sections⁸ give uncertainties in the calculated charge-state fractions. The upper curves were calculated using the largest capture and smallest ionization cross sections, and the lower curves were calculated using the lowest capture and highest ionization cross sections within the experimental uncertainties. The shapes of these curves are determined by an interplay between the Z_t dependence of the capture and ionization cross sections. The ionization cross sections vary approximately as Z_t^2 and the REC cross sections increase linearly with Z_t . At low Z_t , REC is dominant, and the equilibrium fractions decrease with Z_t because ionization becomes relatively more effective than capture with increasing Z_t (Fig. 3). At intermediate Z_t , the NRC cross sections increase more steeply with Z_t than ionization, so the equilibrium fractions increase. Finally, at high Z_t , the NRC cross sections increase less rapidly with Z_t , so the equilibrium fractions level off. The calculated fractions are in good agreement with experiment.

Also shown in Fig. 5 are the results of the ground-state-model calculation of equilibrium charge states. The main difference between the ground-state and the 11-state results is in the He-like fractions. The ground-state model gives 20%–60% larger He-like fractions, which is outside of the liberal theoretical uncertainties in the ground-state calculations. This result is qualitatively consistent with gas-solid differences in equilibrium charge states noted at lower energies.^{1–3} For $Z_p = 54$, the average solid-target projectile charge state, $54F_0 + 53F_1 + 52F_2 = 53.85$ at $Z_t \sim 13$, is larger than the ground-state model or gas-target charge state, 53.71.

The quasiground-state model for equilibrium charge states agrees with the numerical 11-state calculations within about 5% for all Z_t . The difference between the ground-state and thick-target equilibrium fractions is thus confirmed to be due to the lower effective excited-state capture cross sections and slightly larger effective ionization cross sections.

B. The target-thickness dependence of the charge-state fractions

One of the purposes of constructing models of the present complexity is to answer the following question: What does one measure when one determines effective capture and ionization cross sections from thick-target measurements? In many experiments, incident several-electron ions are used, and charge-state fractions are measured as a function of the target thickness, from very small to equilibrium thicknesses.¹ One least-squares fits the measured charge-state fractions to solutions of differential equations such as those given in Eq. (8) by varying the cross sections, thereby obtaining some kind of best-fit, effective ionization, s_1 and c_1 , and capture, a_1 and $a_2 + a_3$, cross sections. Since we have shown that our model gives reasonable equilibrium charge-state fractions and, as shown below, $K\alpha$ and K REC x-ray production cross sections, we can now perform numerical experiments. We shall calculate zero-, one-, and two-electron fractions as a function of target thickness using the 11-

state model, and we will fit the numerical results to the ground-state models, Eq. (8), like experimentalists¹ to see how the resulting effective charge-changing cross sections relate to the physical ground-state values.

Figure 6 shows the calculated target-thickness dependence in 197-MeV/amu Xe + Ag collisions for incident Xe^{52+} ions in the $1s^2$ state. At low T , F_1 increases as s_1T , F_0 increases as c_1T , and F_2 falls off with T . At high T , each fraction approaches the equilibrium values shown in Fig. 5.

The dashed lines in Fig. 7 show ratios of charge-state fractions $F_{j,gs}$, calculated with the ground-state model [Eq. (8)] and with ground-state cross sections, to the 11-state results shown in Fig. 6, $F_{j,11}$, for $j=0, 1$, and 2 electrons. The ratios are nearly unity at small thicknesses, but $F_{2,gs}/F_{2,11}$ approaches 1.5 at large thicknesses, in agreement with the calculated equilibrium charge-state fractions shown in Fig. 5. This calculation confirms that for thin solid targets one can, by fitting F_1 to s_1T and F_0 to c_1T , obtain the ground-state ionization cross sections. This, indeed, was the basis of our ground-state ionization and capture cross-section measurements.⁸ We used the 11-state model to simulate the measurements of the ionization and capture cross sections in a number of other thin solid-target measurements described in paper III.⁸ The simulations confirm the validity of the experimental method used in those experiments. One always obtains the ground-state cross sections in the region where the target-thickness dependence of the charge-state fractions is linear. Excited-state effects do not appear until larger thicknesses are used.

Least-squares fits of the calculated 11-state charge-state fractions in Fig. 6 were made by solving the differential equations in Eq. (8) for incident He-like ions. The cross sections in Eq. (8) were varied following the least-squares grid-search procedure described by Bevington.³⁰ We obtain the following for the final best-fit cross sections $\bar{\sigma}$:

$$\begin{aligned} \bar{s}_1 &= 1.05s_1, \quad \bar{c}_1 = 1.05c_1, \\ \bar{a}_1 &= 1.02a_1, \quad \bar{a}_2 + \bar{a}_3 = 0.559(a_2 + a_3). \end{aligned} \quad (23)$$

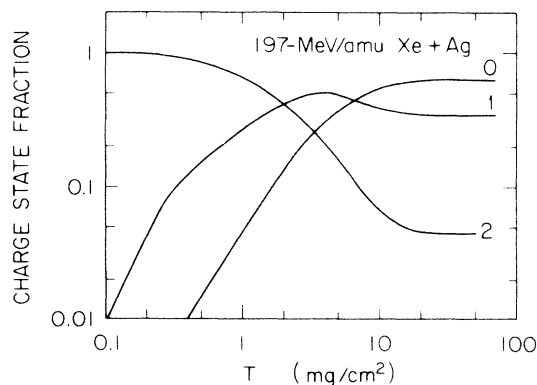


FIG. 6. Calculated target-thickness dependence of zero-, one-, and two-electron charge-state fractions for incident Xe^{52+} ions in 197-MeV/amu Xe + Ag collisions, calculated using the 11-state model.

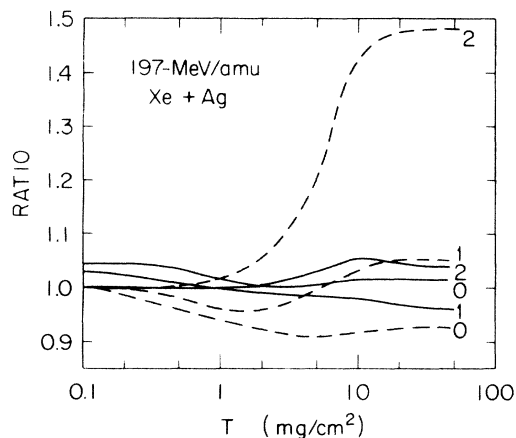


FIG. 7. Dashed lines represent ratios of solutions to the ground-state model, Eq. (8), using ground-state cross sections, to the 11-state results shown in Fig. 6. The solid lines are ratios of solutions to Eq. (8), using best-fit effective cross sections $\bar{\sigma}$ given in Eq. (23), to the 11-state results.

The ratios of the calculated best-fit charge-state fractions $F_{j,\text{fit}}$ to the 11-state results are shown by solid lines in Fig. 7.

The least-squares fitting procedure attempts to compromise between what is needed to fit the small- and large-target-thickness behavior. In the grid-search procedure we used the ground-state cross sections as an initial guess, so that in the first iteration the major error for which the least-squares fit attempted to compensate is in the difference between $F_{2,\text{gs}}$ and $F_{2,11}$. The least-squares-fit program brings $F_{2,\text{fit}}$ into closer agreement with $F_{2,11}$ by decreasing $a_2 + a_3$ and increasing s_1 and c_1 . To fit the equilibrium value of $F_{2,11}$, the quasiground-state model implies that $a_2 + a_3$ should be decreased according to

$$\bar{a}_2 + \bar{a}_3 = r_2 a_2 + r_3 a_3 \approx 0.55(a_2 + a_3) \quad (24)$$

and that \bar{s}_1 and \bar{c}_1 should be a factor $r_s = 1.08$ higher than the ground-state values. If one increases \bar{s}_1 and \bar{c}_1 by a factor of 1.08, however, the F_1 and F_0 fractions at low T , which increase as $s_1 T$ and $c_1 T$, are then incorrect, so that the least-squares procedure has to compromise by letting \bar{s}_1 and \bar{c}_1 be only a factor 1.05 higher than the ground-state values. The final values of $F_{1,\text{fit}}$ and $F_{0,\text{fit}}$ are about 1.05 times higher than the 11-state results at low T , and $F_{2,\text{fit}}$ is 1.04 times too high at large T .

These simulations point out a serious flaw in thick-target determinations of charge-changing cross sections. The least-squares determination gives best-fit cross sections which are a compromise between the effective charge-changing cross sections at small and large target thicknesses. There are no experimental uncertainties in the present "numerical data," and the points are spread uniformly (on a logarithmic scale) from low to high thicknesses. In any actual measurement, one is liable to have a sparser and less precise data set, and the fitted cross sections may depend on the relative number of points at low versus high target thicknesses. Unfortunately, in actual measurements, one often uses incident five- to

ten-electron ions, which the present model cannot address quantitatively.

C. X-ray and radiative capture photon cross sections

Figure 8 compares measured and calculated $K\alpha$ x-ray production cross sections. The 197-MeV/amu cross sections were calculated using the 11-state and quasiground-state models (which give the same results within about 1%), and the 82-MeV/amu cross sections were calculated using the quasiground-state model including three- and four-electron projectiles. The major theoretical uncertainties in the present models come from the uncertainties in the $2p$ capture cross sections. If, on one extreme, we assume that no capture goes into the $n=2$ states, we obtain the lower curves in Fig. 8. If we assume that all of the Xe^{52+} capture goes into the $2p$ state, we get the upper curves. The relative $2p$ capture contributions calculated using the eikonal (for NRC)²³ and impulse (for REC)⁷ approximations give the middle curves which are in good agreement with experiment. At 82 MeV/amu, the measured cross sections are slightly larger than the theoretical predictions at low Z_t , where the equilibrium thickness is so large that the ion loses a significant amount of energy in the target. The observed charge-state fractions and x-ray production cross sections there correspond to a lower mean ion energy, which we have not taken into account.

The main contribution to $K\alpha$ x-ray production comes from the excitation of $1s$ electrons to the $2p$ state followed by $2p \rightarrow 1s$ decay, as shown in Fig. 9. In 197-MeV/amu Xe collisions, $2p$ capture and the $2s \rightarrow 2p$ contributions each account for about 10% of the $K\alpha$ x-ray cross sections. In 82-MeV/amu Xe collisions, $1s$ ionization of three- and four-electron projectiles accounts for about

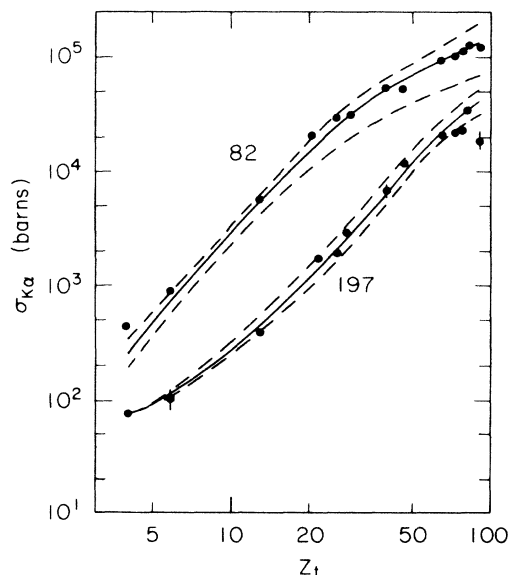


FIG. 8. Measured and calculated Xe $K\alpha$ x-ray production cross sections in 82- and 197-MeV/amu collisions. The uncertainties in the fraction of the Xe^{52+} electron capture into $2p$ states gives theoretical uncertainties extending from the lower to upper dashed lines.

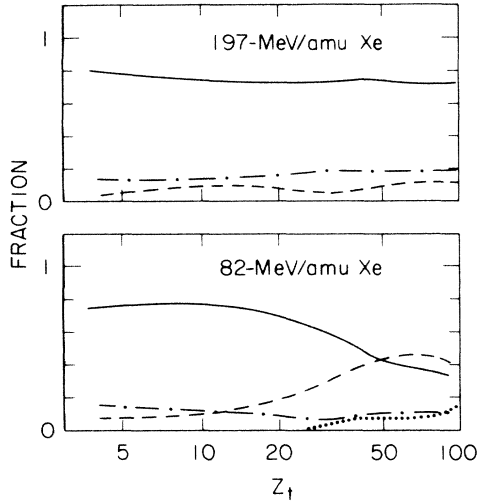


FIG. 9. Relative contributions to projectile $K\alpha$ x-ray production due to $1s \rightarrow 2p$ excitation (solid lines), $2p$ capture (dashed lines), $2s$ capture plus $1s 2s$ excitation (dot-dashed lines), and $1s$ ionization in three- and four-electron projectiles (dotted line).

10% of the cross section at large Z_t . The dominance of the $1s$ excitation contributions is clearly seen in the shape of the $K\alpha$ x-ray production curve at 197 MeV/amu. The cross sections vary as the product of the electron number $F_1 + 2F_2$, which varies like the S-shaped curves in Fig. 5, and the excitation cross sections, which increase as Z_t^2 .

The K REC photon cross sections are defined as

$$\sigma_{K \text{ REC}\gamma} = \frac{N_{Kv}}{2} \sigma_{K \text{ REC}}, \quad (25)$$

where $\sigma_{K \text{ REC}}$ is the REC cross section into empty projectile K shells. In Ref. 7, we noted that the K REC photon cross sections give a measure of the number of equilibrium K vacancies N_{Kv} carried by the projectile inside solid targets. These can be compared with the present post-target charge-state measurements. Since doubly excited states usually are not formed in the present zero-, one-, or two-electron high- Z ions, post-target Auger decay^{1,3} cannot increase the charge states. Hence, the post-target and REC photon measurements are expected to give identical K -vacancy fractions. The inset in Fig. 5 shows that this is indeed the case for 197-MeV/amu Xe ions. At high Z_t , the REC measurements are most uncertain due to bremsstrahlung background.

V. CONCLUSIONS

This paper represents one culmination of our studies of relativistic heavy-ion-atom collisions. The fundamental studies of capture and ionization processes discussed in the previous papers have been applied here to calculate the complex interactions occurring inside solid targets, which determine projectile charge states and projectile x-ray production. We have verified the assertion made in the introduction to this paper and in earlier ones:^{4,24} When relativistic ions are studied, the ionization, excitation, decay, and capture cross sections generally can be calculated accu-

ately and in sufficient detail so that one can begin to predict details about the states of ions in matter. The plane-wave Born approximation for ionization and excitation and the eikonal approximation for NRC are not sufficiently accurate in every case, but experimental information can be used to normalize the calculations.

For the present high- Z ions, the charge states of ions emerging from solid targets should be slightly higher than those from gas targets, in agreement with results at nonrelativistic velocities.¹⁻³ This is seen in the lower measured values of the two-electron charge-state fractions than predicted using the ground-state cross sections. For low- Z relativistic projectiles, the fraction of ions bearing electrons is reduced due to larger effective ionization cross sections, because $1s \rightarrow 2s$ and $1s \rightarrow 2p$ excitation processes leave the projectile in excited states that are easily ionized.⁴ For heavy projectiles, dipole excitation leads to the rapid dipole-allowed decay back to the ground state. The smaller two-electron charge-state fractions for high- Z ions are caused by capture into metastable states, which does not always lead to attachment. Those electrons are easily ionized, giving smaller fractions of ions carrying electrons. Also, this effect is more important for high- Z ions, because capture into excited states is negligible for low- Z relativistic ions, but the excited-state capture cross sections are relatively larger for 82- and 197-MeV/amu Xe ions.⁸

The equilibrium projectile $K\alpha$ x-ray production cross sections depend on several different capture, ionization, and excitation processes which can be calculated quantitatively. The dominant mechanism is $1s$ - $2p$ excitation followed by $2p$ - $1s$ radiative decay.

ACKNOWLEDGMENTS

This work was supported in part by National Science Foundation Grant No. PHY-83-13676. The measurements presented in this paper are the results of collaborations with H. Wegner and P. Thieberger (Brookhaven National Laboratory); H. Bowman, J. O. Rasmussen, H. Gould, Ch. Munger, and J. Alonso (Lawrence Berkeley Laboratory); D. H. H. Hoffman (Gesellschaft für Schwerionenforschung, Darmstadt); Ch. Stoller, J. D. Molitoris, and D. Spooner (Stanford University); S. A. Andriamonje (Université de Bordeaux); E. Morenzoni (Eidgenössische Technische Hochschule, Zürich); and J.-S. Xu and Z.-Z. Xu (Fudan University). We would like to especially thank H. Gould, who was the source of much of the information about He-like and Li-like states.

APPENDIX A: $1s 2s$ - $1s 2p$ EXCITATION

For one-electron ions, $2s \rightarrow 2p$ excitation is discussed in paper II.⁴ In He-like ions, $1s 2s \rightarrow 1s 2p$ excitation is more complicated due to the interplay between electrostatic (electron-electron repulsion) and relativistic (spin-orbit, Darwin terms, etc.) perturbations of the various levels. At low Z , where the relativistic perturbations are small, dipole excitation is limited to transitions with $\Delta S=0$ and $\Delta J=0, \pm 1$. The excitation cross section can be written as

3P_1 , 3P_2 , and 1P_1 are produced with relative probabilities depending on the level multiplicities. Of these, the 3P_1 and 1P_1 decay rapidly giving $K\alpha$ x rays, and we assume the others do not. Thus for $1s$ ionization we obtain

$$\Delta\sigma_{K\alpha} = \frac{3}{4} \frac{1}{12} (3\omega_2 + 3\omega_3) 2s_1 = \frac{3}{8} s_1 (\omega_3 + \omega_1). \quad (\text{B1})$$

For $1s \rightarrow 2p$ excitation in Li-like ions, we get the following from the $1s^2 2p$ configuration: $2x_2 \frac{3}{4} \frac{5}{6} \omega_1$, where the factor $\frac{5}{6}$ accounts for the smaller number of $2p$ vacancies and the factor $\frac{3}{4}$ is for the relative population of $1s^2 2p$ states. For the $1s^2 2s$ configuration, we get $2x_2 \frac{1}{4} \omega_1$, giving

$$\Delta\sigma_{K\alpha} = \frac{7}{4} x_2 \omega_1. \quad (\text{B2})$$

The possible decay of the additional $2p$ electron in the $1s^2 2p$ configuration is not included, which would increase $\Delta\sigma_{K\alpha}$ slightly.

In the Be-like ions the initial configuration is expected to be

$$\frac{1}{16} (1s^2 2s^2) + \frac{6}{16} (1s^2 2s 2p) + \frac{9}{16} (1s^2 2p^2).$$

For excitation, one obtains, using the same arguments as for the Li-like excitation,

$$\begin{aligned} \Delta\sigma_{K\alpha} &\approx \left(\frac{1}{16} 2x_2 + \frac{6}{16} 2x_2 \frac{5}{6} + \frac{9}{16} 2x_2 \frac{4}{6} \right) \omega_1 F_4 \\ &= \frac{3}{2} \omega_1 x_2 F_4. \end{aligned} \quad (\text{B3})$$

For ionization, the analysis of the many-fold states populated after $1s^2 2s^2$, $1s^2 2s 2p$, or $1s^2 2p^2$ $1s$ ionization, each with its diverse solid-target fluorescence yield, is beyond simple analysis. We thus use

$$\Delta\sigma_{K\alpha} \approx 2s_1 F_4 \quad (\text{B4})$$

which assumes a high probability of $K\alpha$ decay.

¹H. D. Betz, *Rev. Mod. Phys.* **44**, 465 (1972).

²N. Bohr and J. Lindhard, *K. Dan. Vidensk. Selsk. Mat.-Fys. Medd.* **28**, No. 7 (1954).

³H. D. Betz and L. Grodzins, *Phys. Rev. Lett.* **25**, 211 (1970).

⁴R. Anholt, *Phys. Rev. A* **31**, 3579 (1985) (paper II).

⁵P. Thieberger, H. E. Wegner, J. Alonso, H. Gould, R. Anholt, and W. E. Meyerhof, *Proceedings of the Particle Accelerator Conference, Vancouver, British Columbia, 1985* [IEEE Trans. Nucl. Sci. **N532**, 1767 (1985)].

⁶H. Gould, D. Greiner, P. Lindstrom, T. J. M. Symons, and H. Crawford, *Phys. Rev. Lett.* **52**, 180 (1984).

⁷R. Anholt, S. A. Andriamonje, E. Morenzoni, Ch. Stoller, J. D. Molitoris, W. E. Meyerhof, H. Bowman, J.-S. Xu, Z.-Z. Xu, J. O. Rasmussen, and D. H. H. Hoffmann, *Phys. Rev. Lett.* **53**, 234 (1984).

⁸W. E. Meyerhof, R. Anholt, J. Eichler, H. Gould, Ch. Munger, J. Alonso, P. Thieberger, and H. E. Wegner, *Phys. Rev. A* **32**, 3291 (1985) (paper III).

⁹R. Anholt, W. E. Meyerhof, Ch. Stoller, E. Morenzoni, S. Andriamonje, J. D. Molitoris, O. K. Baker, D. H. H. Hoffmann, H. Bowman, J.-S. Xu, Z.-Z. Xu, K. Frankel, D. Murphy, K. Crowe, and J. O. Rasmussen, *Phys. Rev. A* **30**, 2234 (1984) (paper I).

¹⁰R. Anholt, W. E. Meyerhof, H. Gould, Ch. Munger, J. Alonso, P. Thieberger, and H. E. Wegner, *Phys. Rev. A* **32**, 3302 (1985) (paper IV).

¹¹E. Merzbacher and H. N. Lewis, in *Corpuscles and Radiation in Matter II*, Vol. 34 of *Encyclopedia of Physics*, edited by S. Flügge (Springer, Berlin, 1958), p. 111.

¹²G. S. Khandelwal, B.-H. Choi, and E. Merzbacher, *At. Data* **1**, 103 (1969).

¹³R. Anholt, *Phys. Rev. A* **17**, 1009 (1979).

¹⁴G. Basbas, W. Brandt, and R. Laubert, *Phys. Rev. A* **17**, 1655 (1978).

¹⁵J. H. McGuire, *Phys. Rev. A* **26**, 143 (1982).

¹⁶M. R. C. McDowell and J. P. Coleman, *Introduction to Ion-Atom Collisions* (North-Holland, Amsterdam, 1970), p. 139.

¹⁷J. T. Park, J. E. Aldag, J. M. George, and J. L. Peacher, *Phys. Rev. A* **14**, 608 (1976).

¹⁸J. T. Park, *Adv. At. Mol. Phys.* **19**, 67 (1982).

¹⁹H. A. Bethe and E. E. Salpeter, *Quantum Mechanics of One- and Two-Electron Atoms* (Academic, New York, 1957).

²⁰C. D. Lin, W. R. Johnson, and A. Dalgarno, *Phys. Rev. A* **15**, 154 (1977).

²¹R. M. Pratt, A. Ron, and H. K. Tseng, *Rev. Mod. Phys.* **45**, 273 (1973).

²²R. Anholt and J. Eichler, *Phys. Rev. A* **31**, 3505 (1985).

²³J. Eichler, *Phys. Rev. A* **32**, 112 (1985).

²⁴R. Anholt, *Nucl. Instrum. Methods B* **10**, 49 (1985).

²⁵H. J. Crawford, Ph.D. thesis, University of California, Berkeley, 1979.

²⁶F. Bell, H. D. Betz, J. Panke, W. Stehling, and E. Spindler, *J. Phys. B* **9**, 3017 (1976).

²⁷S. K. Allison, *Rev. Mod. Phys.* **30**, 1137 (1958).

²⁸J. M. Hansteen, O. M. Johnsen, and L. Kocbach, *At. Data Nucl. Data Tables* **15**, 306 (1975).

²⁹H. D. Betz (private communication).

³⁰P. R. Bevington, *Data Reduction for the Physical Sciences* (McGraw-Hill, New York, 1969) (GRIDL program).

³¹D. H. Sampson and R. E. H. Clark, *Astrophys. J. Suppl. Ser.* **44**, 169 (1980).